

# Prospects of negative triangularity tokamak for advanced steady-state confinement of fusion plasmas

Linjin Zheng, M. T. Kotschenreuther, F. L. Waelbroeck,

M. E. Austin, W. L. Rowan, P. Valanju, and X. Liu

*Institute for Fusion Studies, University of Texas at Austin, Austin, TX 78712*

(Dated: January 30, 2024)

## Abstract

The steady-state confinement, beta limit, and divertor heat load are among the most concerned issues for toroidal confinement of fusion plasmas. In this work, we show that the negative triangularity tokamak has promising prospects to address these issues. We first demonstrate that the negative triangularity tokamak generates the filed line rotation transform more effectively. This brings bright prospects for the advanced steady-state tokamak scenario. Given this, the stability and confinement features of negative triangularity tokamak are investigated. We point out that the negative triangularity configuration with a broad pressure profile is indeed more unstable for low- $n$  magnetohydrodynamic modes than the positive triangularity case so that the H-mode confinement can hardly be achieved in this configuration, where  $n$  is the toroidal mode number. Nevertheless, we found that the negative triangularity configuration with high bootstrap current fraction, high poloidal beta, and peaked pressure profiles can achieve higher normalized beta for low- $n$  modes than the positive triangularity case. In a certain parameter domain, the normalized beta can reach about twice the extended Troyon limit, while the same computation indicates that the positive triangularity configuration is indeed constrained by the Troyon limit. This shows that the negative triangularity tokamaks are not only favorable for divertor design to avoid the edge localized modes but also can have promising prospects for advanced steady-state confinement of fusion plasmas in high beta.

PACS numbers: 52.53.Py, 52.55.Fa, 52.55.Hc

## I. INTRODUCTION

The steady-state confinement, beta limit, and divertor heat load are among the most concerned issues for toroidal confinement of fusion plasmas. These issues depend sensitively on the equilibrium configurations, positive or negative triangularity. In conventional tokamaks, including ITER [1], the positive triangularity configuration is chosen. This is mainly because the H-mode confinement — an operating mode with high energy confinement — can be achieved in this type of configurations [2]. This seems to be favorable for the stability in high beta confinement. Here, beta ( $\beta$ ) represents the ratio between plasma and magnetic pressures. However, it is gradually realized that the divertor heat load is a major concern for the H-mode confinement. This is because the H-mode confinement is often tied to the damaging edge localized modes (ELMs) [2]. ELMs can discharge particles and heat into the scrape-off layer and subsequently to the divertors. The divertor plates can be damaged by such a discharge.

The negative triangularity tokamak is proposed as a possible solution [3–5]. When the divertor configuration is moved from the high field side in the positive triangularity case to the low field side in the negative triangularity case, a larger separatrix wetted area is achieved due to the larger major radius of divertor location. With the divertor in the low field side, a larger room is yielded for divertor engineering design. However, as discussed in Refs. 6–9, the stability beta limit is a concern for negative triangularity tokamaks. One can hardly achieve the H-mode confinement in the negative triangularity configuration.

However, there is an important development. Recent TCV and DIII-D experiments found that the low (L) mode discharges in the negative triangularity experiments can reach about the same level of normalized beta as the H mode confinement in the positive triangularity tokamaks [3, 4]. Here, the normalized beta  $\beta_N^{geo}$  is defined as  $\langle\beta\rangle/I_N$ , where  $\langle\beta\rangle$  is the ratio of the volume-averaged plasma pressure to the toroidal vacuum magnetic pressure at the geometric center of plasma column,  $I_N = I/aB$  (MA/m/T) is the normalized toroidal current,  $I$  is the toroidal plasma current,  $B$  is the vacuum toroidal magnetic field at the geometric center,  $a$  is the minor radius. This definition is used in DIII-D experiments [10]. It is slightly different from the original definition  $\beta_N^{Troyon}$  in Refs. 11 and 12, in which  $\langle\beta\rangle^{Troyon}$  is defined as the ratio of the volume-averaged plasma pressure to the volume-averaged toroidal magnetic pressure. Since they are L-mode discharges, there are no ELMs.

Furthermore, the turbulence level is also found to be considerably low in these discharges [3, 4, 8]. This has further stimulated the interest in the negative triangularity tokamaks and motivates us to further explore the concept of negative triangularity tokamaks.

In the equilibrium, we focus on examining the safety factor value difference between the positive and negative triangularity tokamaks. Using the analytic Solovév equilibrium [13], DIII-D-homologous configuration, and the advanced steady-state confinement scenario with high bootstrap current fraction, high poloidal beta, and peaked pressure profiles or the case with internal transport barrier, we found that the negative triangularity tokamak is more effective in generating the field line rotation transform.

Note that both analytic Solovév equilibrium and DIII-D homologous configurations yield lower safety factors in negative triangular configurations. This leads us to promote an advanced steady-state scenario with high bootstrap current fractions. We found that even when the bootstrap current fraction reaches as high as 95%, the achievable case with the numerical equilibrium codes, the safety factor value in the edge region remains reasonably low. This opens promising prospects for the steady-state confinement in the negative triangularity configuration.

In the pressure profile optimization, we note that the H mode can hardly be achieved in the negative triangularity configuration. This is because the negative triangularity configuration with a broad pressure profile is usually more unstable for low- $n$  modes than the positive triangularity case. We also note that the numerical simulation in Ref. [14] shows that the negative triangularity configuration cannot well confine trapped ions. The experimental observation also indicates that the negative triangularity configuration needs higher density for divertor detachment [15]. Furthermore, as we will see that the high local  $q$  region is narrower in the negative triangularity configuration, which is shown in Ref. 16 to be unfavorable to the X-point stabilization of edge modes. All of these point to that the negative triangularity configuration favors the peaked pressure profiles or the case with internal transport barrier. A further reason that leads us to consider the pressure profile to be more peaky than that of the L-mode type is due to the specific stability properties discussed next.

Based on these interesting features, the magnetohydrodynamic (MHD) stability of the advanced steady-state confinement scenario with high bootstrap current fraction, high poloidal beta, and peaked pressure profiles or internal transport barrier in the negative triangularity configuration is investigated. We found that the advanced negative triangularity scenario

can achieve a higher normalized beta for low- $n$  modes than the positive triangularity case [10]. In a certain parameter domain, the normalized beta limit can reach about  $8 l_i(I/aB)$  for low- $n$  modes, about twice the extended Troyon limit for conventional positive triangularity tokamaks. This good stability property is attributed to the equilibrium feature that the steep pressure gradient appears in the core region where the magnetic shear is negative, while the safety factor near the edge region remains to be low. This leads us to conclude that the negative triangularity tokamaks have promising prospects for advanced steady-state confinement of fusion plasmas in high beta.

The paper is arranged as follows: In Sec. II the negative triangularity equilibria are explored to show its effectiveness in generating the field line rotation transform. The Solovév equilibrium, the DIII-D-homologous equilibria, and the advanced steady-state scenario are examined. In Sec. III, the MHD stability both of the DIII-D-homologous equilibria and the advanced steady-state scenario is studied. The conclusions and discussion are given in the last section.

## II. EQUILIBRIUM: LOW SAFETY FACTOR FEATURE OF NEGATIVE TRIANGULARITY CONFIGURATION

One of the key challenges for tokamaks is steady-state confinement. The toroidal confinement requires the field-line rotation transform. In tokamaks, it is realized by inducing the toroidal plasma current using the transformer principle with plasma working as the secondary coil. Due to the current saturation of the primary coil, one cannot hold the tokamak Ohmic current steadily. For steady-state confinement, the bootstrap current or other current drive means are resorted to. We found that the negative triangularity configuration is more effective in generating the field-line rotation transform, i.e., reducing the safety factor.

We consider the axisymmetric tokamak configuration. In this case, the magnetic field can be expressed as follows

$$\mathbf{B} = \nabla\phi \times \nabla\chi + f(\chi)\nabla\phi, \quad (1)$$

where  $f$  denotes the poloidal current density flux. One can arbitrarily introduce a poloidal angle  $\theta_{eq}$  here. Introducing the so-called flux coordinates, for example, the PEST coordinates

[17], Eq. (1) is transformed to

$$\mathbf{B} = \nabla\phi \times \nabla\chi + q(\chi)\nabla\chi \times \nabla\theta_p, \quad (2)$$

where  $\phi$  is the axisymmetric toroidal angle,  $\chi$  is the poloidal magnetic flux,  $q(\chi)$  denotes the safety factor, and  $\theta_p$  is the poloidal angle. In the so-called PEST coordinates, one has

$$\begin{aligned} \theta_p &= \frac{f}{q} \int_0^{\theta_{eq}} d\theta_{eq} \frac{\mathcal{J}}{X^2}, \\ q &= \frac{f}{2\pi} \oint d\theta_{eq} \frac{\mathcal{J}}{X^2}, \\ \mathcal{J} &= \frac{1}{\nabla\phi \times \nabla\chi \cdot \nabla\theta_{eq}}. \end{aligned} \quad (3)$$

$$\mathcal{J} = \frac{1}{\nabla\phi \times \nabla\chi \cdot \nabla\theta_{eq}}. \quad (4)$$

One can derive the Grad-Shafranov equation for an axisymmetric system. In cylindrical coordinates  $(X, Z, \phi)$ , it can be expressed as

$$X \frac{\partial}{\partial X} \frac{1}{X} \frac{\partial \chi}{\partial X} + \frac{\partial^2 \chi}{\partial Z^2} = -\mu_0 P'_\chi X^2 - f f'_\chi,$$

where  $X$  is the major radius,  $Z$  is the height,  $\mu_0$  is the magnetic constant,  $P$  is the pressure, and the prime denotes the derivative with respect to  $\chi$ .

We examine both the Solovév analytical equilibrium and numerical equilibria. For numerical equilibria, we use the VMEC code as the Grad-Shafranov equation solver [18], with the bootstrap current being included from the Sauter formula [19], to extensively construct the tokamak equilibria. The toroidal current profile in the Grad-Shafranov equation is determined self-consistently by specifying the density and temperature profiles. When the temperature and density profiles are given, the pressure is determined. Also, since the plasma resistivity depends on temperature, the Ohmic current is then determined by the given temperature profile. The bootstrap current is also determined by the given density and temperature profiles. By iteration, the amount of Ohmic current is varied to yield a specified total current (bootstrap plus Ohmic). In this process, the amount of the Ohmic current is varied consistently with the neoclassical conductivity. Both DIII-D-homologous and advanced steady-state scenarios are investigated numerically. The DIII-D-homologous equilibria have been used for stability analyses as reported in Refs. 7 and 8. Here, we focus on discussing their safety factor features.

### A. Solovév equilibrium

In this subsection, we examine the Solovév equilibrium [13]. The Solovév equilibrium solution also allows us to explore the triangularity effects on the safety factor semi-analytically. In the Solovév equilibrium, one assumes that

$$-\mu_0 P'_\chi = a \quad \text{and} \quad -f f'_\chi = b X^2. \quad (5)$$

We consider the exact Solovév equilibrium solution as given as follows

$$\chi = [(b + c_0)X_0^2 + c_0(X^2 - X_0^2)] \frac{Z^2}{2} + \frac{1}{8}(a - c_0)(X^2 - X_0^2)^2, \quad (6)$$

where  $X_0$  denotes the major radius of magnetic axis,  $a$ ,  $b$ , and  $c_0$  are constant parameters. In order to determine the cross section and for the safety factor calculation, we first determine the separatrixes of the solution in Eq. (6). They are obtained by the stationary points of  $\chi$ :

$$\begin{aligned} \frac{\partial \chi}{\partial Z} = 0 &\rightarrow X^2 - X_0^2 = -\frac{b + c_0}{c_0} X_0^2, \\ \frac{\partial \chi}{\partial (X^2 - X_0^2)} = 0 &\rightarrow Z^2 = -\frac{1}{2} \frac{a - c_0}{c_0} (X^2 - X_0^2). \end{aligned}$$

From them, one can determine the parameters

$$\frac{a}{c_0} = 1 - 2 \frac{Z_s^2}{X_s^2 - X_0^2}, \quad \frac{b}{c_0} = -1 - \frac{X_s^2 - X_0^2}{X_0^2}, \quad (7)$$

where  $(X_s, Z_s)$  are the X-point coordinates. Using Eq. (7), let us now consider the case with a quasi-mirror symmetry of positive and negative triangularity cases, i.e.,  $X_0^2 - X_{sp}^2 = X_{sn}^2 - X_0^2$ , where the subscripts  $p$  and  $n$  are introduced to denote the positive and negative triangularity cases, respectively. One therefore has

$$\frac{a_n}{c_{0n}} = 2 - \frac{a_p}{c_{0p}}, \quad \frac{b_n}{c_{0n}} = -2 - \frac{b_p}{c_{0p}}.$$

We have extensively examined the general feature of safety factor in the Solovév equilibria. Here, let us discuss the case with the DIII-D-like geometric parameters. We choose  $X_0 = 1.67$ ,  $X_{sp} = 1.05$ ,  $Z_{sp} = 1$ , and the beta at the magnetic axis  $\beta_0 = 0.03$ . In this case, the quasi-mirror-symmetric positive and negative triangularity Solovév equilibria can be determined. The equilibrium cross sections are plotted in Fig. 1, with the  $\beta$  and  $f$  profiles given respectively in Figs. 2 and 3. From Eq. (6) one can see that  $c_0^2$  can be absorbed into the definitions of  $a$  and  $b$ . We therefore choose  $c_0 = 1$  for simplicity.  $a = -0.1860$

and  $b = -1.6047$  in the negative triangularity case and  $a = 2.1860$  and  $b = -0.3953$  in the positive triangularity case. Here, it should be pointed out that in determining  $f$  from  $b$  there is an integration constant, which is actually related to the magnitude of toroidal field, The integration constant is therefore used to scale the beta value at the magnetic axis.

The safety factor can be computed for the equilibria shown in Fig. 1 respectively for positive and negative triangularity cases. The results are plotted in Fig. 4. Because at the X point,  $|\nabla\chi|$  vanishes. The Jacobian in Eq. (4) becomes infinite. Consequently, as is well known the surface-averaged safety factor becomes infinite on the last closed flux surface as shown in Fig. 4. From the definition of the safety factor in Eq. (3) one can see that the safety factor is a surface-averaged quantity. Noting that the Jacobian only becomes singular at the X points, one can expect that the integrand in the definition of safety factor, Eq. (3), is not singular everywhere. This leads us to plot out the local safety factor profiles,  $q_{local} = \mathcal{J}f/X^2$ , in Fig. 5.

Let us now discuss some interesting features of the safety factor in the positive and negative triangularity cases. First, from Figs. 4 and 5 one can see that both of the surface-averaged and local safety factors in the negative triangularity case are lower than that in the positive triangularity case. This is also seen in our VMEC equilibrium calculations with the bootstrap current taken into account to be described later on.

Next, as pointed out in our recent work in Ref. 20, the equilibrium with X point on the plasma edge occurs only if the included angle of plasma segment is 90 degrees. Otherwise, the X point is present in the vacuum region and the plasma-vacuum interface becomes a hyperbola near the X point. A thin plasma edge layer needs to be truncated off to form a hyperbola type of boundary with the X point located in the vacuum region. From Figs. 4 and 5 one can see that such a truncation affects the edge  $q$  more in the negative triangularity case than in the positive one. Furthermore, from Fig. 5 one can see that the surface-averaged  $q$  as shown in Fig. 4 may not be a relevant quantity to describe the X-point effects on the MHD modes. The local  $q$  depends on the poloidal location. This leads Ref. 16 to introduce the dual-poloidal-region  $q$  description. In this description, the X-point stabilization is more extensive in the positive triangularity case than in the negative triangularity case since its high  $q$  region is more extensive in the radial direction. In Ref. [14] it is shown that the trapped ions can hardly be confined in the negative triangularity configuration. Therefore, the negative triangularity configuration has a stronger radial electric field. Nonetheless, the

H-mode can hardly be achieved in the negative triangularity case. Also, the density for the divertor detachment in the negative triangularity case is required to be higher [15]. It indicates that the edge transport in the L mode confinement in the negative triangularity configuration is still strong. With the X-point stabilization effects discussed in Ref. 16, one may explain why the H mode can occur in the positive triangularity case, instead of the negative one. This is because the positive triangularity configuration contains a larger high local  $q$  region. This leads the MHD modes to be stabilized in the pedestal region. This leads us to conclude that the equilibrium with the internal transport barrier or peaked pressure profile is preferred in the negative triangularity case. This is also consistent with the experimental observations in TCV and DIII-D [3, 4] that the negative triangularity configuration favors the L mode confinement. We push further to consider the case with an even more peaked pressure profile.

In passing, it is also interesting to point out that there is a limitation to generating the Solovév equilibria with negative triangularity. This is because both  $P'_\chi$  in Eq. (5) and  $\chi$  in Eq. (6) by definitions depend on the parameter  $a$ . To ensure the pressure profile is monotonically decreasing in the radial direction, the elongation cannot be too small. For example, the solution does not exist if  $Z_s = 0.9$  in the Fig. 1 case. The negative triangularity case in Fig. 1 is achieved by a negative  $a$  and monotonically decreasing  $\chi$ , for the parameters mentioned above. This does not mean that the small elongation equilibrium does not exist in the negative triangularity case since a homogeneous solution can be added in. How this phenomenon affects the stability of negative triangularity configuration without a large elongation remains to be investigated. Coincidentally, the advanced steady-state scenario to be introduced later on is indeed further elongated.

## B. DIII-D-homologous equilibria

In this subsection, we discuss the DIII-D-homologous negative triangularity equilibria. The equilibria have been used for stability analyses in Refs. 7 and 8. Here, we focus on discussing the safety factor feature of the negative triangularity configuration as compared to the positive one.

The experimental results for DIII-D negative triangularity discharges were reported in Ref. [4]. As explained in Refs. 7 and 8, the experimental equilibrium is numerically



reconstructed by the EFIT code [21]. The toroidal magnetic field at the geometry center is  $B_T = 2\text{T}$ , the total current is fixed to be  $I = 0.9\text{MA}$ , and the major and minor radii are respectively  $R = 1.67\text{m}$  and  $a = 0.6\text{m}$ . To extend the parameter domain outside the experimental values in DIII-D, we numerically construct the DIII-D-homologous equilibria with positive, zero, and negative triangularity:  $\delta = 0.4, 0.0,$  and  $-0.4$ . The L-mode pressure profile is used to simulate DIII-D experiments. The procedure has been reported in Refs. 7 and 8 and also outlined at the beginning of this section. The typical cross sections of the positive and negative triangularity configurations of DIII-D-homologous equilibria are given in Fig. 1 of Ref. 8. The main equilibrium parameters are summarized in Table I, in which  $\delta$  denotes triangularity,  $\beta_N^{geo}$  is the normalized beta as used in the DIII-D experiments,  $\beta_N^{Troyon}$  is the normalized beta introduced by Troyon,  $\langle\beta\rangle$  is the volume-averaged beta,  $l_i$  is the inductance per unit length, and  $f_{bs}$  represents the bootstrap current fraction.

TABLE I: Equilibrium parameters

Case	PT1	PT2	NT1	NT2
$\delta$	0.4	0.4	-0.4	-0.4
$\beta_N^{geo}$	3.79	4.74	2.68	3.38
$\beta_N^{Troyon}$	3.35	4.23	2.73	3.47
$\langle\beta\rangle$ (%)	2.84	3.55	2.01	2.53
$l_i$	0.705	0.600	0.806	0.702
$f_{bs}$ (%)	53	66	43	53

To show the safety factor features of positive and negative triangularity configurations, the pressure (or  $\beta$  normalized by the magnetic field at the axis) and safety factor profiles for positive and negative triangularity cases given in Table I are plotted in Figs. 6 and 7, respectively. Again, by comparing Figs. 6 and 7 one can see that the negative triangularity configuration leads to a lower safety factor value  $q$ , especially near the edge. Note that both positive and negative triangularity equilibria are created with the same total toroidal current and toroidal magnetic field. The low  $q$  feature leads us to explore the possibility of steady-state confinement in the negative triangularity configuration in the next subsection.

### C. Advanced steady-state confinement scenario

In this subsection, we examine the advanced steady-state scenario in the negative triangularity configuration [7]. As shown in the Solovév equilibrium and the DIII-D-homologous cases, the negative triangularity configuration is shown to be more effective in creating the field line rotation transform as compared to the positive triangularity configuration with the same given toroidal current and toroidal magnetic field. This motivates us to explore the advanced steady-state scenario with a high bootstrap current fraction in the negative triangularity configuration.

Since this is new, we are no longer bound to the DIII-D configurations. Instead, we consider the configuration with the elongation  $\kappa = 2$  and aspect ratio being 3 as often employed for steady-state tokamak studies. We mainly investigate the negative triangularity configurations, while a comparison with the positive case is also made. The typical cross-sections for positive ( $\delta = 0.4$ ) and negative ( $\delta = -0.4$ ) triangularity configurations are shown in Fig. 8.

In further exploring the equilibrium parameter domain, we found that the negative triangularity favors the peaked pressure profiles; while the positive triangularity the broad pressure profiles. This leads us to consider the cases with high bootstrap current fraction, high poloidal beta, and peaked pressure profiles. We consider five negative triangularity cases with  $\delta = -0.4$ . Their equilibrium parameters are given in Table II and the pressure and safety factor profiles are given in Figs. 9 and 10, respectively. The equilibrium sequences are generated by raising up the center pressure. In these cases, the magnetic field is 2T, the total toroidal current is 1.2MA, and the minor radius is 0.6m. From Table II one can see that the bootstrap current fraction is very high in these equilibrium cases. We cannot generate equilibrium cases with even higher bootstrap current fraction because the loop between the Grad-Shafranov equation solver and the subroutine for computing bootstrap current tends to become hard to converge. The Mercier stability status is also given in Table II, which will be discussed in subsection III B. They are the cases with an internal transport barrier.

Again, it is important to point out that the negative triangularity configuration is so effective in generating the field line rotation transform that the low edge  $q$  feature is insensitive to raising the bootstrap current fraction. This can be seen in Fig. 10. In particular, in this figure one can see that the  $q$  value near the plasma edge remains to be low even for

TABLE II: Equilibrium parameters

	Case 1	Case 2	Case 3	Case 4	Case 5
$\beta_0(\%)$	11.5	11.9	12.3	12.7	13.1
$\langle\beta\rangle(\%)$	3.60	3.86	4.12	4.41	4.60
$\beta_N^{geo}$	3.60	3.86	4.12	4.41	4.60
$\beta_N^{Troyon}$	3.71	3.98	4.27	4.58	4.79
$l_i$	0.708	0.674	0.639	0.602	0.585
$4(I/aB)$	4	4	4	4	4
$4l_i(I/aB)$	2.84	2.68	2.56	2.40	2.34
$f_{bs}(\%)$	80	82	85	88	95
Mercier	(0.20,0.35)	(0.24,0.33)	stable	stable	stable

the case with the bootstrap current fraction being 95%.

### III. THE ADVANCED STABILITY FEATURES OF NEGATIVE TRIANGULARITY TOKAMAKS

In this section, we investigate the MHD stability of the negative triangularity tokamaks. Both the DIII-D-homologous equilibria and the advanced steady-state confinement scenario are investigated. In Sec. II, we have shown that the negative triangularity configuration is more effective in generating the field line rotation transform. We will show that the negative triangularity configuration can also be good for stability. The results are reported in several conferences, including the 27th IAEA Fusion Energy Conference [7]. The low  $n$  mode stability features of DIII-D-homologous equilibria were reported in Refs. 8 and 9 to show the comparison with the intermediate  $n$  modes and to study the rotation and diamagnetic effects. To compare with the advanced steady-state confinement scenario, the DIII-D-homologous cases are reviewed here with further details reported.

For stability, we investigate the low- $n$  MHD stability using the AEGIS code [22]. AEGIS is a linear ideal MHD stability code. It uses the Fourier decomposition in the poloidal direction and independent solution decomposition in the radial direction. Adaptive shooting is used

to obtain the independent solutions. AEGIS has been developed for several years. Here, let us briefly discuss its benchmarks with other MHD codes. The benchmarks with other major MHD codes in this field were performed when it was developed [22], for example, GATO [23]. It has been benchmarked with other codes in the last decade. Very recently, its comparison with MISHKA for Alfvén calculation is also shown to give a good agreement [24]. Nevertheless, since rather high beta stability is found in the AEGIS numerical computation for negative triangularity tokamaks, we employ the DCON code [25] as a double check. The results obtained in the AEGIS calculations are found to be consistent with the DCON results. Besides, we also study the localized mode stability: the Mercier criterion and ballooning mode stability using the codes in the DCON package. This is the usual procedure for developing a new concept. The conformal wall is used in our calculations.

#### **A. Stability of DIII-D-homologous equilibria**

To compare with the advanced steady-state confinement scenario in Subsection III B, in this subsection, we outline the MHD stability results of DIII-D-homologous equilibria. The equilibria have been described in subsection II B. They are based on the DIII-D experimental g-file with the extrapolation to the positive and negative configurations with various beta values. Considerable results were reported in Ref. 8. Here, we add more details and some further results.

We first study the DIII-D negative triangularity discharges using the q-file. Our stability analyses using the AEGIS code, together with DCON, confirm that the equilibrium with the normalized beta of 2.6 achieved in DIII-D experiments is stable against the  $n = 1$  MHD kink modes with critical wall position  $b = 1.18$  and  $n = 2, 3$  modes with the critical wall position 1.05. DIII-D is not originally configured for negative triangularity discharges, the last closed flux surface touches the inner wall and the X-points are close to the outer part of the wall in the negative triangularity experiments. Given that a large volume of magnetic flux touches the wall and the parallel mobility of electrons, as an estimate we believe the case is not far from the fixed boundary scenario. This is different from the DIII-D positive triangularity discharges, where the wall is much further from the plasma. Note that the inner wall becomes effectively a limiter and the outer part of the wall distance is about 1.2 with the X-points close to the wall. Our results about the critical wall positions seem to be

consistent with the experimental observation.

To investigate the DIII-D-homologous numerical equilibria as described in Subsection II B, we also use the AEGIS code, together with DCON. It is found that for the same given density and temperature profiles, the positive triangularity case is best, the zero triangularity case remains in the middle, and the negative triangularity case is worst for  $n = 1$  MHD mode stability. While the normalized beta limit is reduced considerably in the negative triangularity cases, it nonetheless still remains reasonably high. This can be seen from the numerical results summarized as follows [8]. For each normalized beta  $\beta_N^{geo}$  we compute the critical wall positions for different triangularity cases. The system is more stable if the critical wall position is larger. Table III shows the critical wall position  $b_c$  versus the normalized beta  $\beta_N^{geo}$  for three different triangularity cases, Actually, the profiles given in Figs. 6 and 7 are related, respectively, to the stability conditions in Table III : The profiles in Fig. 6 correspond to the positive triangularity cases with  $(b_c = 1.51, \beta_N^{geo} = 3.79)$  and  $(b_c = 1.21, \beta_N^{geo} = 4.74)$ ; the profiles in Fig. 7 correspond to the negative triangularity cases with  $(b_c = 1.86, \beta_N^{geo} = 2.68)$  and  $(b_c = 1.05, \beta_N^{geo} = 3.38)$ .

TABLE III: Critical wall position versus  $\beta_N^{geo}$

Case	PT1	PT2	PT3	OT1	OT2	NT1	NT2	NT3
$\delta$	0.4	0.4	0.4	0.0	0.0	-0.4	-0.4	-0.4
$\beta_N^{geo}$	3.79	4.36	4.74	3.11	3.32	2.68	3.14	3.38
$b_c$	1.51	1.28	1.21	1.46	1.31	1.86	1.14	1.05

In Ref. 8, we also studied the intermediate  $n$  mode stability in the negative triangularity case with the DIII-D-homologous equilibria. It is found that although the low  $n$  modes are more unstable in the negative triangularity case, the intermediate- $n$  modes with a resistive wall are more stable in the negative triangularity case than in the positive triangularity case [8]. This is consistent with the experimental observations of the lower level of turbulent transport in the negative triangularity case in TCV and DIII-D experiments [3, 4].

In Ref. 9, we also studied the rotation and diamagnetic drift effects on the  $n = 1$  modes in the negative triangularity case with the DIII-D-homologous equilibria. It is found that although the low  $n$  modes are more unstable in the negative triangularity case, the rotation

and diamagnetic drift stabilization effects are more effective in the negative triangularity case than in the positive triangularity case [9].

### B. Stability property of the advanced steady-state confinement scenario

In this subsection, we study the stability of the negative triangularity equilibria in the advanced steady-state scenario described in subsection II C. We have shown that the negative triangularity equilibria in the advanced steady-state scenario with high bootstrap current fraction, high poloidal beta, and peaked pressure profiles have a favorable equilibrium property in that it can effectively generate the field line rotation transform. In this subsection, we show that the advanced steady-state scenario also has outstanding stability properties. The tendency in the DIII-D-homologous equilibria with a low bootstrap current fraction that the positive triangularity configuration is more stable, as described in Table III in subsection III A, is reversed. The negative triangularity configuration in this scenario becomes more stable than the positive triangularity case.

We first study the cases with an internal transport barrier as shown in Fig. 9. One can first see the favorable stability features of the advanced steady-state scenario from the Mercier criterion shown in Table II. In Table II, the unstable regions in various cases are indicated by the normalized poloidal flux range. The Mercier interchange modes become largely stable as beta increases, possibly because the Grad-Shafranov shift increases or the negative magnetic shear region becomes wider. Here, it is noted that the Mercier stability in Cases 3, 4, and 5 excludes the vicinity of the magnetic axis. The Mercier instabilities usually appear at the vicinity of the magnetic axis. In three cases, they are roughly located inside  $\chi < 0.002$ . They may only cause the local pressure profile to flatten at the magnetic axis.

All five equilibrium cases in Table II are no-wall stable to the  $n = 1, 2, 3$  external kink modes. We have specially studied Cases 4 and 5 since their beta values are high. The  $n = 4$  modes are also no-wall stable for Case 4. The critical wall position for  $n = 5$  modes is 2.53, which is big noting the geometry parameters shown in Fig. 8 (the wall is about touching the axisymmetric axis). Since the numerical equilibrium for Case 5 is marginally acceptable in convergency, we cannot pursue higher  $n$  mode calculations. Since the self-consistent equilibrium computation involves both the MHD equilibrium and the bootstrap current

computations, one has to balance these two for convergency. This makes the VMEC run cannot achieve its highest accuracy in the high bootstrap current percentage case, otherwise, the recalculated bootstrap current would differ from the original bootstrap current input.

Note that  $q_{\min}$  raises from below 2 to above 2 from Case 1 to 5 as shown in Fig. 10. We especially plot the total plasma and vacuum energies for  $n = 2$  modes for the five equilibria in Case 1-5 in Fig. 11. One can see that, when  $q_{\min}$  increases above 2, the  $n = 2$  mode stability improves substantially.

We have also studied the MHD ballooning stability conditions. The unstable regions in the poloidal flux range for Case 3-5 are respectively as follows: (0.36, 0.59), (0.38, 0.68), and (0.61, 0.75). One can see that the unstable region is shifted outward as the beta and bootstrap current fraction increase. From Fig. 9 one can see that for Case 5 the unstable region lies actually at the foot of the internal transport barrier. This may be good for maintaining the peaked pressure profile. Also, since the magnetic shear is low, we expect the kinetic effects can play a role. Therefore, we have not tried to further optimize the pressure profiles for ballooning mode stability. Instead, it is proposed for future studies with kinetic and nonlinear turbulence effects included.

From these results for negative triangularity configuration, one can see that the normalized beta can reach as high as about twice the extended Troyon limit (Case 5) for low- $n$  modes. It also exceeds the usual Troyon limit  $4(I/aB)$ . This high beta stability for negative triangularity configurations with high bootstrap fraction and high poloidal beta is observed in various peaked pressure profiles, including with or without an internal transport barrier. The reasons for good stability features of the negative triangularity equilibria with high bootstrap current fraction and peaked pressure profile are as follows: First, from Figs. 9 and 10 one can see that the pressure gradient is mostly confined in the negative magnetic shear region, which is self-generated by the high bootstrap current; In the corresponding positive triangularity case, instead, the rotation transform is significantly lower, leading to poor stability. Second, note that the negative triangularity configuration tends to have a bigger bad curvature volume. However, this happens mostly in the outer part of plasma column. This adverse feature is minimized by the peaked pressure profile, which places the pressure gradient at a lower negative triangularity region. These contribute to the better stability features achieved for low- $n$  modes.

Note that the Troyon limit for the positive triangularity case was developed primarily

based on the eigenvalue codes and the evaluation of the Mercier/ballooning stability. This method is extended to the negative triangularity cases, for example, Ref. [6]. Reference [6] uses the KINX code. Similar to the KINX code, we use the eigenvalue code: AEGIS. To use AEGIS is because it is an adaptive code, which is good for studying marginal stability. Due to the importance of the current results we use the DCON code for double check. AEGIS and DCON are both radially adaptive codes, based on the shooting from the vicinity of magnetic axis to the plasma edge. Generally speaking, DCON can get the marginal stability, while the eigenvalue codes usually have the limitation on the lowest growthrate to be able to reach. Since AEGIS is an adaptive code, its detectable lowest growthrate is lower than the nonadaptive codes. Therefore, the AEGIS and DCON results are reasonably close for stability calculations. We are especially interested in the high beta cases. For Cases 4 and 5 we see the so-called internal “zero crossing” phenomenon with DCON computation, which may indicate that the fixed-boundary modes are unstable, while AEGIS runs do not see the instabilities. But, our extra check shows that they do not converge with respect to how small the starting  $\chi$  is and how many sidebands are used in DCON runs themselves. The stability and instability appear alternatively (for example, with sidebands 10 is unstable, 12 is stable, and 14 is unstable again...). The uncertainty on the internal mode “zero crossing” in the high beta equilibria with Mercier interchange mode being stable is not because the DCON is an unreasonable code, nor because the convergency has not been checked. This indicates that even if the most stringent energy minimization code DCON is used for double check, no reliable unstable kink modes are found. We believe that this numerical uncertainty may be because they are too close to the marginal stability so the stability conditions become sensitive to the numerical parameters. Note that the ideal MHD theory is inapplicable for the too small growthrate cases. The non-ideal MHD effects, like the finite Larmor radius effect, can play a significant role there. This remains for future studies.

We have also studied the cases without internal transport barrier. Figure 12 shows the pressure and  $q$  profiles for the case without internal transport barrier. The equilibrium parameters are as follows:  $B_T = 2\text{T}$ ,  $I = 1.2\text{MA}$ ,  $a = 0.6\text{m}$ ,  $\beta_N^{geo} = 4.780$ ,  $\beta_N^{Troyon} = 5.016$ ,  $\langle\beta\rangle = 4.780$ ,  $l_i = 0.41$ , and  $f_{bs} = 0.89$ . Its cross-section is given in Fig. 8b. In this case  $I/aB = 1$  and  $4l_i(I/aB) = 1.64$ . The normalized beta  $\beta_N^{geo}$  is about 3 times the extended Troyon limit. We also find that the  $n = 1, 2, 3$  external kink modes are stable in this case. The Mercier interchange modes also are largely stable, except in the vicinity of magnetic axis.



But, the ballooning modes are unstable in the  $\chi$  regions: (0.2841, 0.3120) and (0.428, 0.983). This also shows the good stability potential especially for low  $n$  external modes.

Since we obtained the results with the normalized beta exceeding the Troyon limit, we have been extra cautious to check if the Troyon limit is there for the positive triangularity case. This is a check to the code system, although we have observed the Troyon limit in extensive computing experiences using the AEGIS/DCON system in decades. We indeed verified the Troyon limit in the positive triangularity case. The details are as follows. The negative triangularity equilibria are compared with the positive triangularity configuration with the same type of peaked pressure profiles. No interesting cases are found to exceed significantly the Troyon limit in the positive triangularity cases. A typical equilibrium with positive triangularity  $\delta = 0.4$  is described as follows:  $B_T = 2T$ ,  $I = 1.2MA$ ,  $a = 0.6m$ ,  $\beta_N^{geo} = 3.727$ ,  $\beta_N^{Troyon} = 3.310$ ,  $\langle\beta\rangle = 3.728$ ,  $l_i = 0.62$ , and  $f_{bs} = 0.67$ . Its cross-section is given in Fig. 8a and pressure and q profiles are given in Fig. 13. The stability results are given as follows: The critical wall positions for  $n = 1, 2$  external kink modes are respectively 1.55 and 1.45; while the  $n = 3$  modes are no-wall stable. Compared with the data in Table II, one can see that the positive triangularity equilibrium with a peaked pressure profile is more unstable than the negative one. We have also studied the Mercier and ballooning stability for this positive triangularity case. The system is largely Mercier stable, except in the vicinity of magnetic axis. But, the ballooning modes are unstable in the  $\chi$  regions: (0.0792, 0.0902) and (0.2279, 0.4937).

The results show that the negative triangularity configuration is favorable for steady-state confinement in the advanced tokamak scenario with high bootstrap current fraction, high poloidal beta, and peaked pressure profile. It can achieve an even higher normalized beta than the positive triangularity case. As shown in Fig. 14, in a certain parameter domain, the normalized beta can reach about twice as high as the so-called Troyon limit for positive triangularity tokamaks as given in Ref. 10. The beta value seems to be limited by the high  $n$  ballooning modes for this type of configurations. Nevertheless, the ballooning instabilities occur only at the foot of the transport barrier or the peaked pressure profile. The results show that the advanced steady-state scenario of negative triangularity we developed is not only good for divertor design but also good for steady-state confinement and MHD stability.

## IV. CONCLUSIONS AND DISCUSSION

In conclusion, in equilibrium, we found that the negative triangularity tokamaks are more effective in generating the magnetic field line rotation transform, which especially shows that the negative triangularity tokamak can be very attractive for a steady-state fusion reactor [7–9]. The advanced steady-state scenario reported in this work can work about without an externally driven current while maintaining the safety factor near the plasma edge to be reasonably low.

In stability, we report the results both for the DIII-D-homologous configurations and the advanced steady-state scenario. To compare with the advanced steady-state confinement scenario, we first review the stability studies for the DIII-D-homologous equilibria [7–9]. It is confirmed that the equilibrium in the DIII-D negative triangularity experiments with normalized beta 2.6 and L-mode profile is indeed stable to the low- $n$  MHD modes. We then discuss the three triangularity cases with the triangularity  $\delta = 0.4$ ,  $0.0$ , and  $-0.4$  by extrapolating the DIII-D experimental configurations with L-mode profiles and low bootstrap current fraction. It is found that the positive triangularity case is the most stable, the zero triangularity case remains in the middle, and the negative triangularity case is the most unstable for low  $n$  MHD modes. Nevertheless, the reduction of beta value for the negative triangularity configuration is not dramatic and is still within an acceptable range. Also, it is found that although the low  $n$  modes are more unstable in the negative triangularity case, the intermediate- $n$  modes with a resistive wall are more stable in the negative triangularity case than the positive triangularity case [8]. This is consistent with the experimental observations of the lower level of turbulent transport in the negative triangularity case in TCV and DIII-D experiments [3, 4]. We also pointed out that although the low  $n$  modes are more unstable in the negative triangularity case, the rotation and diamagnetic drift effects are more effective in the negative triangularity case than the positive triangularity case as shown in Ref. 9.

Most importantly, our work shows the promising prospects of negative triangularity tokamak for advanced steady-state confinement of fusion plasmas with high beta. We examine the negative triangularity configurations with high bootstrap current fraction, large poloidal beta, and peaked pressure profiles. We find that the negative triangularity configuration is more stable than the positive triangularity case in this scenario. In a certain parameter

domain, the normalized beta limit can reach about  $8 l_i(I/aB)$  for low- $n$  modes, about twice the extended Troyon limit  $4l_i(I/aB)$  for the conventional positive triangularity tokamaks. The same type of computations confirms that the positive triangularity configuration is indeed constrained by the Troyon limit. Only, the negative triangularity configuration with high bootstrap current fraction, large poloidal beta, and peaked pressure profiles can substantially overcome the Troyon limit. It is known in the earlier works, for example, Ref. [6], that the positive triangularity case is good for H-mode with a broad pressure profile, but the negative triangularity case is not. We find that the negative triangularity favors, instead, the peaked pressure profiles or with internal transport barrier. The good stability potential for negative triangularity configuration with high bootstrap current fraction, large poloidal beta, and peaked pressure profiles results from that the pressure gradient is mostly confined in the negative magnetic shear region, which is self-generated by the high bootstrap current.

Our results indicate that the negative triangularity tokamaks are not only good for divertor design, but also can potentially achieve high beta, steady-state confinement with a very high bootstrap current fraction. This steady-state scenario is good for tokamak fusion reactor. Since the high beta case is achieved with a peaked pressure profile or with an internal transport barrier, one can expect that the performance is ELM-free. The low- $n$  mode stability also implies that the beta limit is determined by the high- $n$  modes and therefore the negative triangularity discharge can have a reduced disruptivity. Since the high beta case is related to the no-wall stability, one can expect a high resistive wall mode beta limit. Also, the peaked pressure profile, favored in the negative triangularity case, can be expected to give rise to higher reactor fusion productivity.

In the end, we would like to point out that the tokamak configuration optimization is an effort in decades and the current work is merely a step forward. More efforts remain to be made in this field to further explore the full potential of the negative triangularity tokamaks. The current investigation is mainly based on the ideal MHD codes, although we did show that the rotation and diamagnetic drift effects are more effective in stabilizing the resistive wall modes in the negative triangularity case. We have followed the conventional procedure in developing a new concept by studying the low  $n$  MHD modes and the Mercier/ballooning mode stability. The results are double-checked with AEGIS and DCON codes. How the non-ideal MHD effects affect the results remains for future studies.

The authors would like to acknowledge Dr. Alan Turnbull for helpful discussions. This

research is supported by the Department of Energy Grants DE-FG02-04ER54742.

---

- [1] Ikeda K, 2007 Progress in the ITER Physics Basis, *Nucl. Fusion* **47**, E01. DOI 10.1088/0029-5515/47/6/E01
- [2] Wagner F. *et al* 1982 Regime of Improved confinement and high beta in neutral-beam-heated divertor discharges of the ASDEX tokamak *Phys. Rev. Lett.* **49** 1408-12.  
<https://doi.org/10.1103/PhysRevLett.49.1408>.
- [3] Camenen Y. *et al* 2007 Impact of plasma triangularity and collisionality on electron heat transport in TCV L-mode plasmas *Nucl. Fusion* **47** 510-16.  
DOI 10.1088/0029-5515/47/7/002.
- [4] Austin M.E. *et al.* 2019 Achievement of Reactor-Relevant Performance in Negative Triangularity Shape in the DIII-D Tokamak *Phys. Rev. Lett.* **122** 115001.  
DOI: <https://doi.org/10.1103/PhysRevLett.122.115001>.
- [5] Kikuchi M., Takizuka T. and Furukawa M. 2014 Negative triangularity as a possible tokamak scenario *JPS Conf. Proc.* **1** 015014.  
<http://sciforum.net/conference/ece-1>.
- [6] Medvedev S. Yu. *et al* 2015 The negative triangularity tokamak: stability limits and prospects as a fusion energy system *Nuclear Fusion* **55** 063013.  
DOI 10.1088/0029-5515/55/6/063013.
- [7] Zheng L.J., Kotschenreuther M.T., Waelbroeck F.L. *et al.* 2018 Negative Triangularity Effects on Tokamak MHD Stability *27th IAEA Fusion Energy Conference*, TH/P1-30
- [8] Zheng L.J., Kotschenreuther M.T. and Waelbroeck F.L. 2021 Intermediate  $n$  mode stability in the negative triangularity tokamaks, *Nuclear Fusion* **61** 116014.  
DOI: 10.1088/1741-4326/ac1a1c.
- [9] Zheng L.J., Kotschenreuther M.T. and Waelbroeck F.L. 2023 “Plasma rotation and diamagnetic drift effects on the resistive wall modes in the negative triangularity tokamaks”, submitted to *Nuclear Fusion*  
DOI: 10.1088/1741-4326/ac1a1c.
- [10] Taylor T. S. *et al* 1991 Profile optimization and high beta discharges, and stability of high elongation plasmas in the DIII-D tokamak *Plasma Physics and Controlled Nuclear*

- Fusion Research* (Vienna: IAEA) **1** p. 177.
- [11] Troyon F., Gruber R., H. Saurenmann H., Semenzato S. and Succi S. 1984 MHD-limits to plasma confinement *Plasma Physics and Controlled Fusion* **26** 209.  
DOI 10.1088/0741-3335/26/1A/319.
- [12] Troyon F. and Gruber R. 1985 A semi-empirical scaling law for the beta-limit in tokamaks *Phys. Lett.* **110A** 29.  
[https://doi.org/10.1016/0375-9601\(85\)90227-0](https://doi.org/10.1016/0375-9601(85)90227-0).
- [13] Solovév, L. S. 1967 The theory of hydrodynamic stability of toroidal plasma configurations *Sov. Phys. JETP* **26** 400. [http://www.jetp.ras.ru/cgi-bin/dn/e\\_026\\_02\\_0400.pdf](http://www.jetp.ras.ru/cgi-bin/dn/e_026_02_0400.pdf).
- [14] Nishimura Y., Waelbroeck F. L., Zheng L. J. 2020 Computational analysis of ion orbital loss in diverted positive- and negative-triangularity tokamaks *Phys. Plasmas* **27**, 012505.  
<https://doi.org/10.1063/1.5131157>.
- [15] Scotti, F. Scrape-Off Layer characterization and detachment integration in Negative Triangularity discharges in DIII-D, *65th Annual Meeting of the APS Division of Plasma Physics, 2023; Denver, Colorado*, VI02.00003.
- [16] Zheng Linjin, Kotschenreuther M. T. , Waelbroeck F. L., and Austin M. E. 2023 X point effects on tokamak edge localized modes in the description of dual-poloidal-region safety factor submitted *Phys. Plasmas*.
- [17] Grimm R. C., Greene J. M., and Johnson J. L., *Methods of Computational Physics* (Academic, New York, 1976).
- [18] Hirshman S. P. and Whitson J. C. 1983 Steepest-descent moment method for three-dimensional magnetohydrodynamic equilibria *Phys. Fluids* **26** 3553-68.  
<http://pof.aip.org/resource/1/PFLDAS/v26/i12>.
- [19] Sauter O., Angioni C. and Lin-Liu Y. R. 1999 Neoclassical conductivity and bootstrap current formulas for general axisymmetric equilibria and arbitrary collisionality regime *Phys. Plasmas* **6** 2834-39.  
<https://doi.org/10.1063/1.873240>.
- [20] Zheng Linjin, Kotschenreuther M. T. , Waelbroeck F. L. 2023 Asymptotic vacuum solution at tokamak X-point tip, *Phys. Plasmas* **30**, 112508.  
<https://doi.org/10.1063/5.0173656>.
- [21] Lao L. L., John H. St., Stambaugh R. D., Kellman A. G. and Pfeiffer W. 1985 Reconstruction

- of current profile parameters and plasma shapes in tokamaks *Nucl. Fusion* **25** 1611-22.  
DOI 10.1088/0029-5515/25/11/007.
- [22] Zheng L.-J. and Kotschenreuther M. 2006 AEGIS: An adaptive ideal-magnetohydrodynamics shooting code for axisymmetric plasma stability *J. Comp. Phy.* **211** 748-66.  
<https://doi.org/10.1016/j.jcp.2005.06.009>.
- [23] Bernard L. C., Helton F. J., and Moore R. W. 1981 GATO: An MHD stability code for axisymmetric plasmas with internal separatrices, *Comput. Phys. Commun.* **24**, 377-380.  
[https://doi.org/10.1016/0010-4655\(81\)90160-0](https://doi.org/10.1016/0010-4655(81)90160-0).
- [24] Oliver H. J. C., Sharapov S. E., Breizman B. N., Zheng L.-J. and JET Contributors 2017 Axisymmetric global Alfvén eigenmodes within the ellipticity-induced frequency gap in the Joint European Torus *Phys. of Plasmas* **24** 122505.  
<https://doi.org/10.1063/1.5005939>.
- [25] Glasser A. H. 2016 The direct criterion of Newcomb for the ideal MHD stability of an axisymmetric toroidal plasma *Phys. Plasmas* **23**, 072505.  
<https://doi.org/10.1063/1.4958328>.

Figure captions

Fig. 1 The cross sections of positive and negative triangularity configurations with the Solovév solutions. The positive triangularity case is plotted in red and negative triangularity in blue.

Fig. 2: The  $\beta$  profiles versus the minor radius on the mid-plane for the positive and negative triangularity configurations as described in Fig. 1. The positive triangularity case is plotted in red and negative triangularity in blue.

Fig. 3: The  $f$  profiles versus the minor radius on the mid-plane for the positive and negative triangularity configurations described in Fig. 1. The positive triangularity case is plotted in red and negative triangularity in blue.

Fig. 4: The surface-averaged safety factor  $q$  profiles versus the minor radius on the mid-plane for the positive and negative triangularity configurations described in Fig. 1. The positive triangularity case is plotted in red and negative triangularity in blue.

Fig. 5: The local safety factor ( $q_{local}$ ) profiles versus the poloidal angle for the positive and negative triangularity configurations as described in Fig. 1. The positive triangularity case is plotted in red and negative triangularity in blue. In each case, the consecutive  $q_{local}$  are plotted from the plasma center to the edge.

Fig. 6. Plasma beta and safety factor profiles versus normalized poloidal magnetic flux  $\chi$  for DIII-D-homologous configuration with the triangularity  $\delta = 0.40$ .

Fig. 7. Plasma beta and safety factor profiles versus poloidal magnetic flux for DIII-D-homologous configuration with the triangularity  $\delta = -0.40$ .

Fig. 8. Cross sections of positive and negative triangularity equilibria in the advanced steady-state tokamak scenario with high bootstrap current fraction. The coordinate  $X$  is the major radius and  $Z$  the height. This figure has been presented in the 27th IAEA fusion energy conference [7]. The copy right for reuse is based on the author right policy by the IOP publishing.

Fig. 9. Pressure profiles versus poloidal magnetic flux for negative triangularity equilibria with the cross section shown in Fig. 8b in the advanced tokamak scenario with high bootstrap current fraction.

Fig. 10. Safety factor profiles versus poloidal magnetic flux for negative triangularity equilibria with the cross section shown in Fig. 8b in the advanced tokamak scenario with high bootstrap current fraction.

Fig. 11. The total perturbation energies for  $n = 2$  modes for five equilibrium cases as given in Table II as computed by DCON. A larger positive  $\delta W$  corresponds to a better stability.

Fig. 12. Plasma beta and safety factor profiles versus normalized poloidal magnetic flux with the triangularity  $\delta = -0.40$  for the configuration with the cross section shown in Fig. 8b. The pressure profile is peaked, but does not have the internal transport barrier.

Fig. 13. Plasma beta and safety factor profiles versus normalized poloidal magnetic flux with the triangularity  $\delta = 0.40$  for the configuration with the cross section shown in Fig. 8a.

Fig. 14. The normalized beta limit for low  $n$  external modes for negative triangularity tokamak configuration in the advanced steady-state scenario, as compared to the experimental observations for the positive triangularity cases (circles or squares). The dashed line is the so-called Troyon limit. Reproduced from Ref. 10 with the negative triangularity results added.



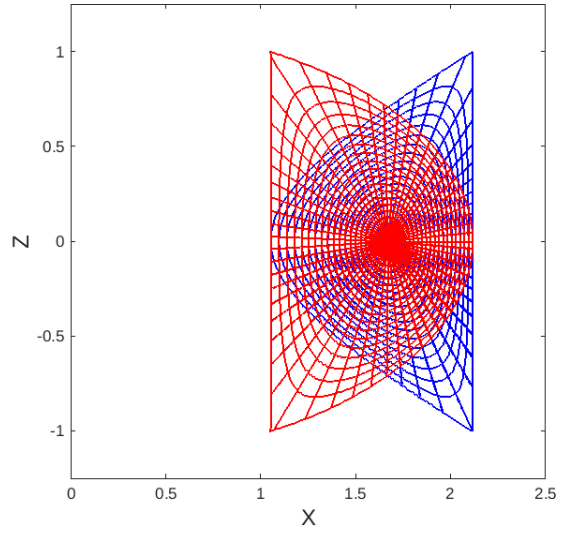


FIG. 1:

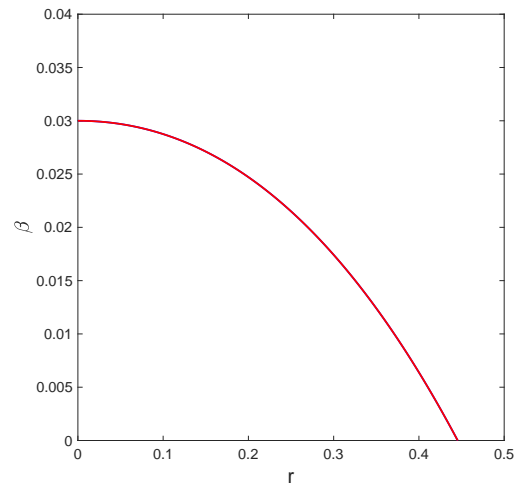


FIG. 2:

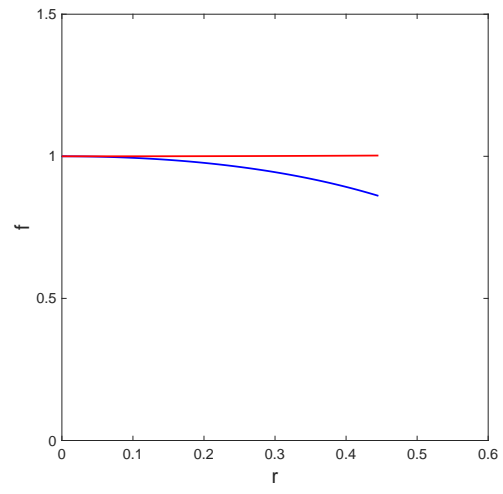


FIG. 3:

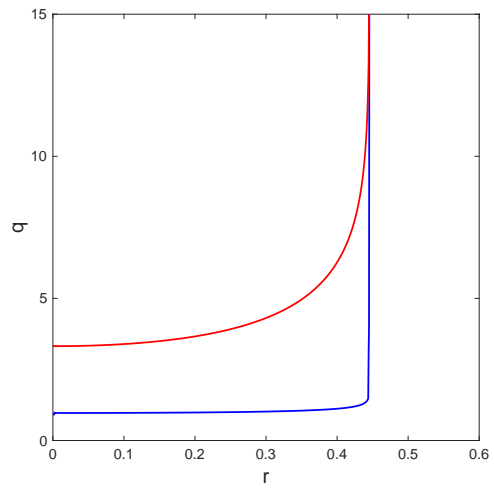


FIG. 4:

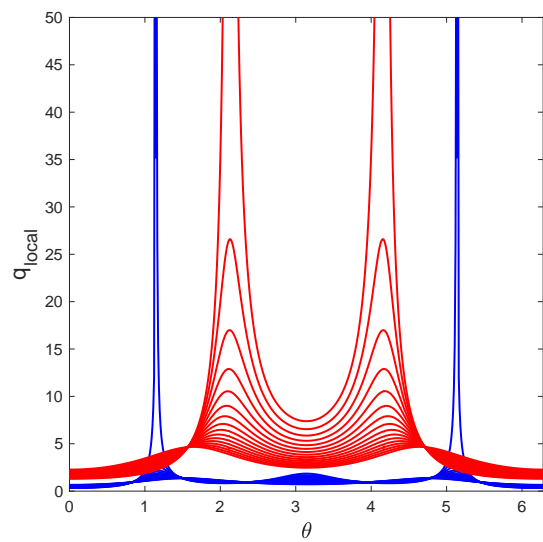


FIG. 5:

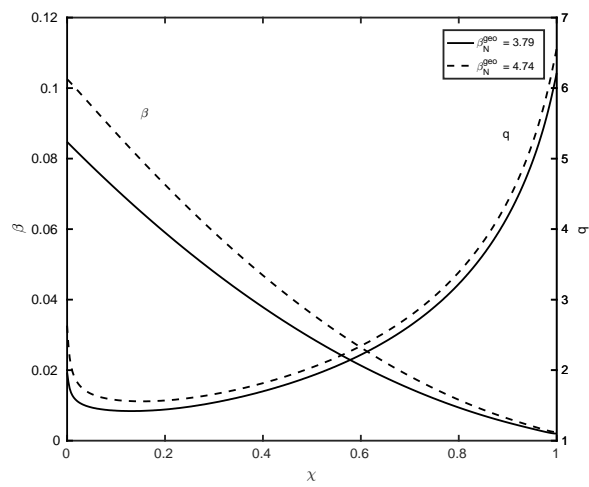


FIG. 6:

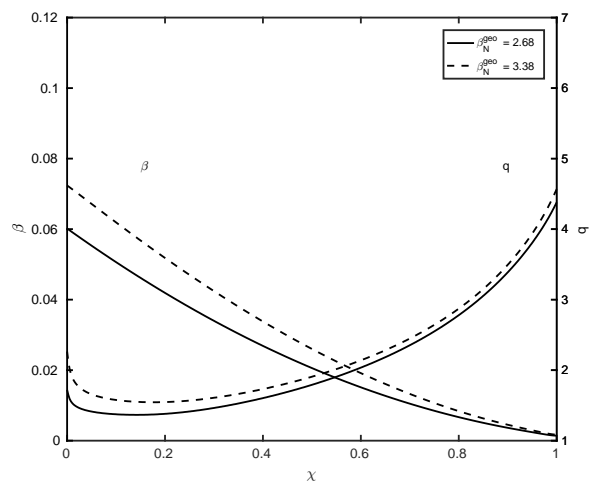


FIG. 7:

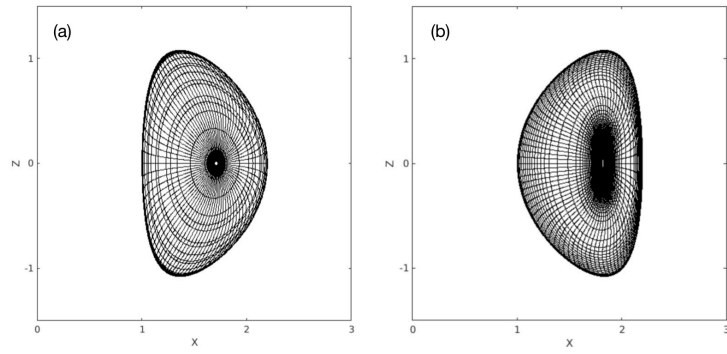


FIG. 8:



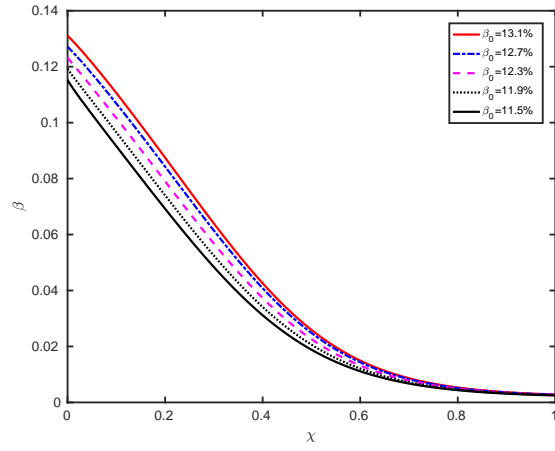


FIG. 9:

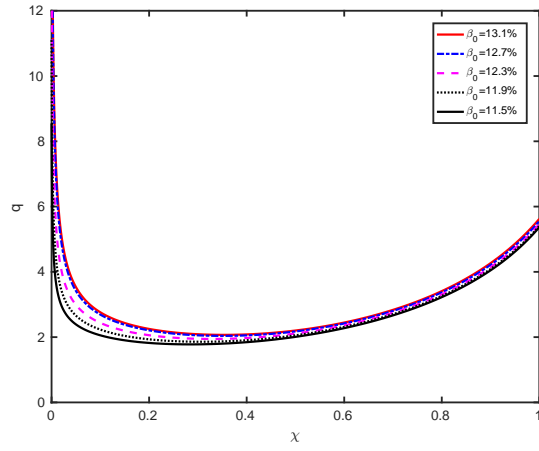


FIG. 10:

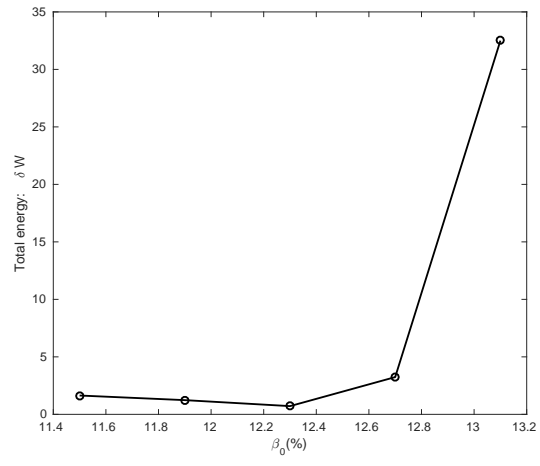


FIG. 11:

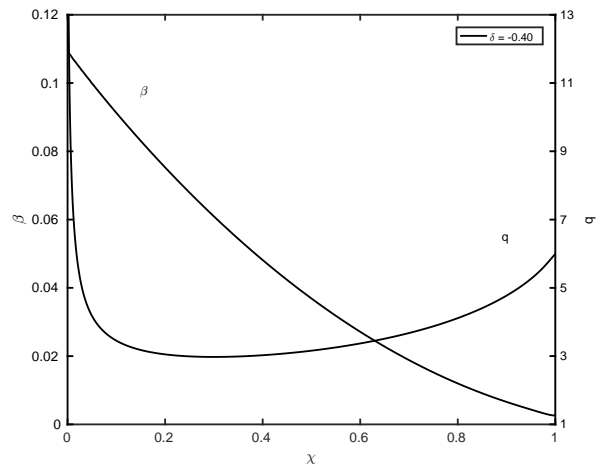


FIG. 12:

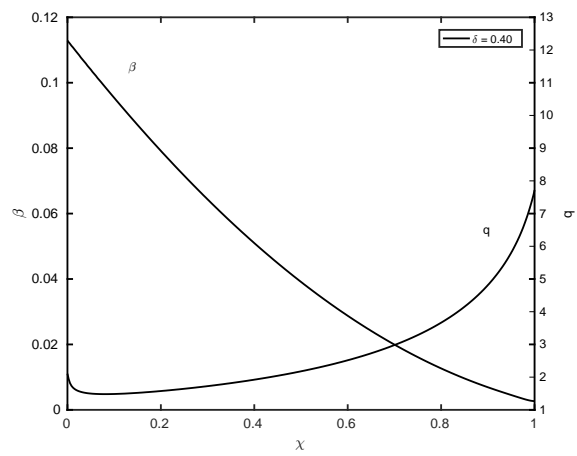


FIG. 13:

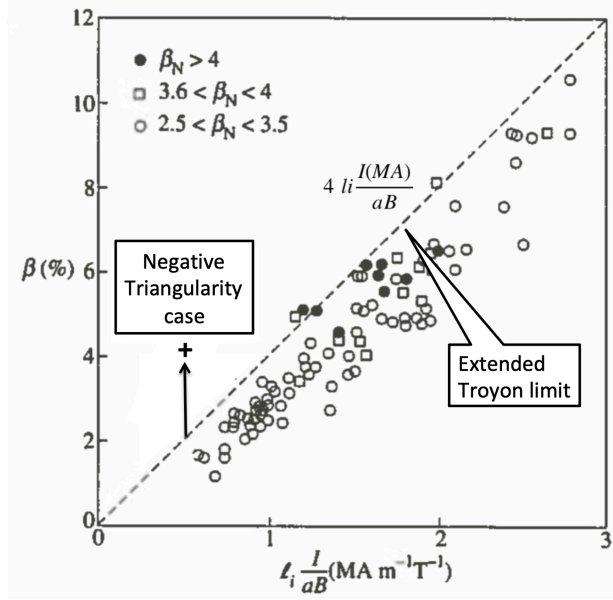


FIG. 14: